Ocean Engineering 309 (2024) 118382

Contents lists available at ScienceDirect

Ocean Engineering

journal homepage: www.elsevier.com/locate/oceaneng

Research paper

Numerical simulation of the vortex shedding and lock-in phenomenon of an active vibration hydrofoil

Pengxiang Zhao [a], Jinliang Wu [a], Xudong Zhang [a], Xin Lan [b], Jinsong Leng [b,**], Yanju Liu [a,*]

[a] Department of Astronautical Science and Mechanics, Harbin Institute of Technology (HIT), P.O. Box 301, No. 92 West Dazhi Street, Harbin, 150001, People's Republic of China

[b] Center for Composite Materials and Structures, Harbin Institute of Technology (HIT), No. 2 YiKuang Street, Harbin, 150080, People's Republic of China

ARTICLE INFO

Keywords:
Vortex shedding
Active vibration
Lock-in
Noise

ABSTRACT

Hydrofoils are widely applied in the maritime domain, and their vibrational characteristics significantly influence the genesis and evolution of vortices. Consequently, modulating vortex shedding through the active vibration of hydrofoils may lead to the enhancement of the hydrodynamic performance of bluff bodies. In order to study the influence of structural oscillations on vortex shedding, both Computational Fluid Dynamics (CFD) and wake oscillator models were used to simulate the modulations of vortex shedding caused by an actively oscillating hydrofoil. By altering the vibration frequency and amplitude, the shedding frequency of vortices can be locked onto the structural vibration frequency. Another important discovery is that the dominant frequency of noise at the trailing edge of the actively vibrated hydrofoil has significantly shifted. Alongside the shift, there is a marked reduction in noise amplitude, denoting a dual acoustical modulation stemming from the vibratory intervention. These advancements provide pivotal contributions to the understanding of fluid-structure interactions and their resultant acoustic phenomena.

1. Introduction

Hydrofoils are critical components of maritime vessels and oceanic structures. As fluid flows around hydrofoils, it recombines at the trailing edge to form regular vortex patterns. When these vortices shed asymmetrically, they generate pulsating pressures that can cause vibrations in the hydrofoil structure. In turn, the vibration of the structure can alter the characteristics of the wake; for instance, when an object is forced into harmonic lateral oscillations, the shedding frequency of the vortices may synchronize with the oscillation frequency of the object, a phenomenon known as a lock-in effect. Due to the significant impact of hydrofoil vibration characteristics on the generation and development of vortices, the study of active vibration of hydrofoils and its modulation on vortex shedding is an important research subject in marine engineering.

Considerable analysis has been carried out by researchers regarding the causes of vortex shedding. Gerard (Gerrard, 1966) found that the separation and convergence of shear layers is a condition for vortex formation and that a vortex that has been dislodged can also pull the opposite shear layer across the mid-axis of the wake to form a new vortex. Griffin (Griffin, 1995) conducted experiments on the vorticity distribution in a cylindrical near wake flow at a low Reynolds number, which helps to understand the process of vorticity generation at high and low Reynolds numbers. Williamson et al. (Williamson and Roshko, 1988) described the multiple modes of vortex shedding caused by cylindrical vibrations and the transition between the different modes.

With deeper research into the mechanisms of vortex formation, researchers have begun to shift the focus to practically significant objects (Du et al., 2023; Nagarathinam et al., 2022; Wang et al., 2023), like hydrofoils. Ausoni (Ausoni et al., 2006) investigated the Kalman vortex shedding process for a two-dimensional hydrofoil with a high Reynolds number. He discovered that vortex shedding could be synchronized to the characteristic frequency of the hydrofoil. Furthermore, the fidelity of unsteady numerical simulations in replicating the vortex shedding frequency was scrutinized. Concordance between the experimental observations and computational results was substantially improved by reducing the discrepancies at critical inflection points within the data sets. Dwayne et al. (Bourgoyne et al., 2005) investigated the near trailing trace fluctuations of a 2D hydrofoil at high Reynolds numbers and found that the variation in near trailing trace vortex shedding

* Corresponding author.
** Corresponding author.
E-mail addresses: lengjs@hit.edu.cn (J. Leng), yj_liu@hit.edu.cn (Y. Liu).

https://doi.org/10.1016/j.oceaneng.2024.118382
Received 30 January 2024; Received in revised form 13 April 2024; Accepted 2 June 2024
Available online 14 June 2024

intensity was related to the Reynolds number and trailing edge geometry. Zobeiri (Zobeiri et al., 2012) found that the sloping trailing edge of the hydrofoil leads to a collision of the shear layers on both sides, which results in a redistribution of vorticity. Ni et al. (2019) experimentally studied the lift-drag properties of slotted hydrofoils near the free surface and compared them with numerical calculations, resulting in a significant improvement in the performance of the surface hydrofoil at large head angles. In addition, researchers have studied the vibration characteristics of hydrofoils, such as the effect of hydrofoil boundary layer transition on hydrofoil vibration (Ducoin et al., 2012), the physical mechanism behind the locking phenomenon (Gao et al., 2017),the normal response of two hydrofoil vortex vibrations (Smith et al., 2021) and the effect of fluid-structure coupling on the cavitation behaviour of flexible hydrofoils (Smith et al., 2020a, 2020b).

In addition to the study of hydrodynamic vibrations, the effects of vibrations of structures on fluids have also been investigated, for example, the control of the shear layer of separation by oscillating the structural body can lead to desired changes in the fluid system (Muhammad et al., 2022; Zhao et al., 2023). Bishop and Hassan (1964) investigated the jump in the phase angle of the force on a cylinder by forcing the cylinder to oscillate in a direction transverse to the free water flow as the oscillation frequency varied around the shedding frequency. Koopman (Koopmann, 1967) also investigated the effect of forced transverse oscillation of the cylinder on vortex shedding and paid particular attention to the variation in the geometry of the wake along the span. Near the upper limit of the control frequency, the transverse spacing of the vortex wake is significantly reduced by the motion of the cylinder. After the mechanism of active control of the flow had been clearly investigated, Warui and Fujisawa (1996) and Tokumaru and Dimotakis (1991) used electromagnetic actuators to effectively reduce the vortex intensity. Actuators are fitted to the two ends of the block to generate movement. Williams et al. (1992) introduced symmetric and asymmetric forces in the cylindrical wake at approximately twice the frequency of vortex shedding through two rows of holes located $\pm 45^{\circ}$ from the stagnation line in front of the column (Re = 470). These researchers successfully modified the vortex street.

Due to the difficulty of theoretical modelling, researchers mostly use numerical simulation to study the trailing edge flow phenomena of hydrofoils (Hu et al., 2020; Lee et al., 2016; Qin et al., 2023). A number of studies on the applicability of turbulence modelling in hydrofoil coiling were carried out by Ye et al. (2020a). In particular, these scholars compared the applicability of LES and DES and analyzed the laminar-to-turbulent transition problem. Zeng et al. (2019) carried out fluid-structure coupling simulation calculations on a NACA0009 three-dimensional hydrofoil under different working conditions to analyze its dynamic characteristics. Huang et al. (2019) conducted hydrodynamic simulations of a rigid hydrofoil and an elastic hydrofoil. The results show that the flexible hydrofoil has less lift and more drag and that its deformation at the leading edge increases.

Taking into account the synchronous shedding of vortices across the hydrofoil's span, (Liu et al., 1996, 2012), a two-dimensional numerical simulation method combined with a wake oscillator model was adopted to study the wake characteristics of an actively vibrating hydrofoil. The focus was on investigating the effects of different vibration conditions on the lateral velocity fluctuations in the hydrofoil's wake. By analyzing flow field diagrams and velocity fluctuation curves, the boundaries of vortex shedding frequency and structural vibration parameters were defined, and the noise characteristics of the trailing edge of the actively vibrating hydrofoil were analyzed.

2. Theoretical analysis and methodology formulation

2.1. Mathematical model

2.1.1. CFD simulation

When considering the Navier–Stokes equations for incompressible homogeneous flow, their mathematical representation is shown through a system of right-angled coordinates as:

$$\frac{\partial u_i}{\partial t}+u_j\frac{\partial u_i}{\partial x_j}=-\frac{1}{\rho}\frac{\partial p}{\partial x_i}+\nu\frac{\partial^2 u_i}{\partial x_i\partial x_j}+f_i, i=1,2,3, \tag{1}$$

$$\frac{\partial u_i}{\partial x_i}=0, i=1,2,3 \tag{2}$$

where ρ denotes the fluid's density, ν signifies the kinematic viscosity coefficient of the fluid, and f_i represents the intensity of the mass force, with $i=1,2,3$ referring to the three degrees of freedom.

The numerical simulations employ the *SST* $k-\omega$ turbulence model, which takes into account the salient features of boundary layer flows with reversed pressure gradients while maintaining inherent computational stability. Its transport equations can be expressed as follows:

$$\frac{\partial(\rho k)}{\partial t}+\nabla\cdot(\rho k\overline{u})=\nabla\cdot\left[\left(\mu+\frac{\mu_t}{\sigma_k}\right)\nabla k\right]+G_k-Y_k+S_k \tag{3}$$

$$\frac{\partial(\rho\omega)}{\partial t}+\nabla\cdot(\rho\omega\overline{u})=\nabla\cdot\left[\left(\mu+\frac{\mu_t}{\sigma_\omega}\right)\nabla\omega\right]+G_\omega-Y_\omega+D_\omega+S_\omega \tag{4}$$

In these equations, the terms G_k and G_ω denote the production of turbulent kinetic energy k and the specific dissipation rate ω, respectively. Likewise, E_k and E_ω denote their effective diffusivity, and σ_k and σ_ω denote their turbulent Prandtl numbers. μ_t is the turbulent viscosity. D_ω is the diffusion part of the equation. S_k and S_ω are customized items.

In fluid calculations, a transition model is a mathematical model used to predict the transition point in fluid flow. The transition point is the location of laminar flow turning into turbulent flow and usually has a significant impact on flow properties, noise and vibration (Ye et al., 2020b).

In contrast to the $\gamma-\mathrm{Re}_\theta$ transition mode, the γ (intermittent) transition mode requires only one transport equation for the turbulent intermittent γ to be calculated and can be used in conjunction with the $\gamma-\mathrm{Re}_\theta$ mode with the following equation:

$$\frac{\partial(\rho\gamma)}{\partial t}+\nabla\cdot(\rho\overline{u}\gamma)=\nabla\cdot\left[\left(\mu+\frac{\mu_t}{\sigma_\gamma}\right)\nabla\gamma\right]+P_\gamma-E_\gamma \tag{5}$$

where P_γ denotes the destruction source. E_γ denotes the transition source term.

The transition model interacts with the *SST* turbulence model by modifying the E_γ equation. Combining the γ model with the *SST* $k-\omega$ model by modifying equation (3):

$$\frac{\partial(\rho k)}{\partial t}+\nabla\cdot(\rho k\overline{u})=\nabla\cdot\left[\left(\mu+\frac{\mu_t}{\sigma_k}\right)\nabla k\right]+G_k^*-Y_k^*+S_k \tag{6}$$

$$\begin{aligned} G_k^* &= \gamma_{eff}G_k \\ Y_k^* &= \min\left(\max\left(\gamma_{eff},0.1\right),1.0\right)Y_k \end{aligned} \tag{7}$$

where G_k and Y_k are original production and destruction terms for *SST* $k-\omega$ equation (3) and γ_{eff} are the correction terms of γ.

2.1.2. Structural boundary deformation

Drawing upon the foundational work of Ausoni and colleagues (Ausoni et al., 2006), it is recognized that the inherent frequency of a hydrofoil can be locked into the frequency of vortex shedding,which is a fundamental feature of flow-excited vibrations. In order to investigate the effect of oscillating hydrofoils on the wake, we first use numerical methods to simulate the lateral fluctuations of the wake with a forced vibration structure and investigate the locking boundary of vortex shedding by varying the frequency and amplitude of the vibrations, as shown in Fig. 1.

The oscillating characteristics of the hydrofoil trailing edge vortex

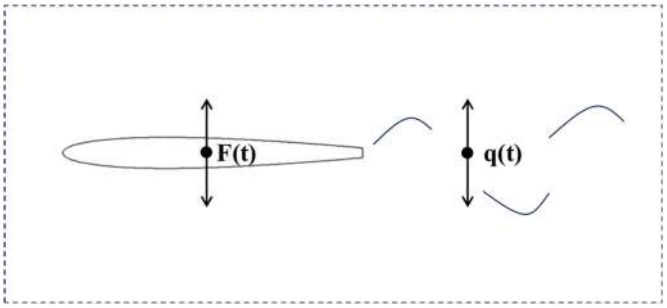

Fig. 1. Model of coupled structure and wake oscillators.

can be modelled with a nonlinear oscillator, which has the following general form:

$$\ddot{q}+\varepsilon\Omega_f\left(q^2-1\right)\dot{q}+\Omega_f^2 q=(A/D)F \tag{8}$$

where ε denotes the damping factor, Ω_f represents the hydrofoil natural vortex shedding frequency and D denotes the hydrofoil characteristic size. The dimensionless wake variable q can be regarded as an implicit flow quantity associated with a weighted mean of the lateral components (Blevins, 1990) or proportional to the lateral speed of a typical near-wake fluid mass (Krenk and Nielsen, 1999). The forced term F represents the forced motion of the structure, for which there are several different coupling models. A represents the coefficient of influence of the forcing term F on the wake, which is generally determined by experiment.

In the CFD simulation, in order to simulate the active vibration of the hydrofoil, the boundary of the structure at t_{n+1} time step is controlled by the following equations:

$$V_{n+1}=a\cdot sin[\omega(t_n+\Delta t)] \tag{9}$$

where V_{n+1} is the structure boundary velocity at t_{n+1} time step, a is the vibration amplitude and ω is the vibration frequency, Δt is the time step interval.

2.1.3. Noise prediction method

The foundational equations governing hydrodynamic noise generation were initially formulated by Sir James Lighthill. Subsequently, the equation developed by Ffowcs Williams and Hawkings (FW-H) extends this framework, providing a generalized acoustic analogy to describe the phenomenon. The equation is based on an integral representation of the area over the source distribution in the acoustic field to predict the noise generated by unsteady flow, which can be derived from the continuity and energy equations of the flow. The equations are as follows:

$$\begin{aligned}\frac{1}{a_0^2}\frac{\partial^2 p'}{\partial t^2}-\nabla^2 p' &= \frac{\partial^2\Omega}{\partial x_i\partial x_j}\left\{T_{ij}H(f)\right\}-\frac{\partial}{\partial x_i}\left\{\left[P_{ij}n_j+\rho u_i(u_n-v_n)\right]\delta(f)\right\}\\ &+\frac{\partial}{\partial t}\left\{\left[\rho_0 v_n+\rho(u_n-v_n)\right]\delta(f)\right\}\end{aligned} \tag{10}$$

where i denotes the direction along coordinate x_i, n denotes the direction normal to the surface $f=0$, u denotes the fluid velocity, v denotes the surface velocity, $\delta(f)$ is the Dirac function, and $H(f)$ is the Heaviside function. a_0 is the far-field sound velocity, P_{ij} is the compressive stress tensor, and T_{ij} is the Lighthill stress tensor. p' is the far-field sound pressure, defined in Eq. (9), which consists of thickness noise $p'_T(x,t)$ and load noise $p'_L(x,t)$.

$$p'(x,t)=p'_T(x,t)+p'_L(x,t) \tag{11}$$

$$\begin{aligned}4\pi p'_T(x,t) &= \int_{f=0}\left[\frac{\rho_0(\dot{U}_n+U_n)}{r(1-M_r)^2}\right]dS\\ &+\int_{f=0}\left[\frac{\rho_0 U_n\left(r\dot{M}_r+a_0\left(M_r-M^2\right)\right)}{r^2(1-M_r)^3}\right]dS\end{aligned} \tag{12}$$

$$\begin{aligned}4\pi p'_L(x,t) &= \int_{f=0}\left[\frac{\dot{L}_r}{r(1-M_r)^2}\right]dS+\int_{f=0}\left[\frac{L_r-L_M}{r^2(1-M_r)^2}\right]dS\\ &+\frac{1}{a_0}\int_{f=0}\left[\frac{L_r\left(r\dot{M}_r+a_0\left(M_r-M^2\right)\right)}{r^2(1-M_r)^3}\right]_{ret}dS\end{aligned} \tag{13}$$

where

$$U_n=\left(v_i+\frac{\rho}{\rho_0}(u_i-v_i)\right)n_i \tag{14}$$

$$L_r=\left(P_{ij}\hat{n}_j+\rho u_i(u_n-v_n)\right)r_i \tag{15}$$

$$L_M=\left(P_{ij}\hat{n}_j+\rho u_i(u_n-v_n)\right)\frac{v_i}{a_0} \tag{16}$$

$$M_r=\frac{v_i}{a_0}r_i \tag{17}$$

where x represents the receiver's position, t is the observer time. ρ_0 is the density of incompressible flow, ρ is the density of compressible flow. r_i and n_i denote the unit vectors in the radiation and wall-normal directions, respectively. The dot over a variable denotes source-time differentiation of that variable.

2.2. Simulation model

We have investigated vortex shedding in two-dimensional vibrating hydrofoils using fluid simulation. Specifically, the NACA0009 hydrofoil is shown in Fig. 2, with a chord length c and trailing edge thickness b of 100 mm and 3.22 mm, respectively. Notably, this model is the same as the one employed in a prior study (Ausoni et al., 2006).

In order to ensure the continuity of the flow simulation, a spacious computational domain was configured based on the research of predecessors (Hu et al., 2020), with a slight increase in height and a reduction in length. The dimensions of the computational domain are specifically 12c × 7c, as shown in Fig. 3. The outlet boundary represents a crucial factor, often heavily influencing the simulation owing to the downstream effects associated with vortex shedding. To mitigate this, the hydrofoil was deliberately situated further from the outlet than the inlet to attenuate the boundary's influence on the simulation results. Furthermore, the inlet's dynamic interaction with the hydrofoil

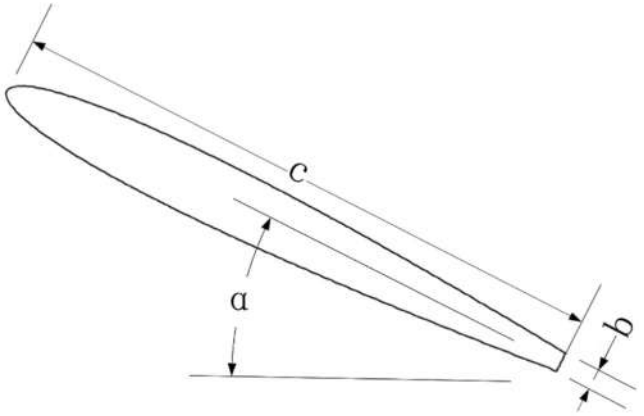

Fig. 2. NACA0009 hydrofoil model.

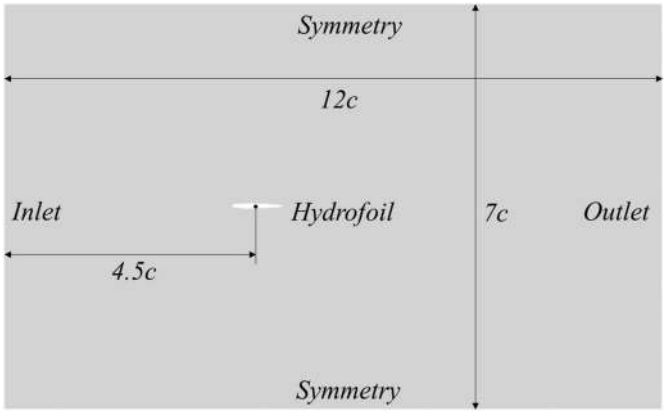

Fig. 3. Computational domain of NACA0009 hydrofoil.

structure was considered negligible. Hence, the inlet was designated as a velocity inlet to promote mass conservation and foster computational stability. Additionally, symmetric boundary conditions were applied to both sides of the computational domain to prevent interference with the vortex shedding simulations associated with the hydrofoil.

In Fig. 4, the discretization of the computational domain for the hydrofoil is presented through the meshing strategy employed. The domain is spatially categorized into two distinct zones: an outer mesh region and a concentrated mesh refinement region proximate to the hydrofoil. The purpose of this local refinement is to capture the intricate flow details near the hydrofoil with enhanced precision; thus, the grid spacing here is reduced to a mere 5% of that in the outer, coarser mesh region. The fluid domain, in total, sums up to 171,180 grid elements. Data transfer between the refinement region and the larger surrounding mesh is facilitated through a well-defined interface, ensuring continuity and accuracy of the computational solution. To optimize computational efficiency and volume, a structured mesh comprising quadrilateral elements is derived via a block-structured meshing technique, as opposed to a less efficient triangular mesh. Such an approach to mesh design not only reduces the number of computational elements required but also serves to enhance the quality of the numerical simulation.

Fig. 4 also showcases the configuration of the near-wall mesh developed for our computational domain. The velocity gradients adjacent to the wall in fluid flow simulations are typically steep, necessitating a denser mesh in these regions to accurately resolve the boundary layer dynamics. Consequently, the mesh refinement near the wall is governed by the non-dimensional wall distance, Y+, which is crucial for our chosen turbulence model, the $SSTk-\omega$ model. Acknowledging the importance of this parameter, we ensure that the Y+ values are kept below the threshold where the boundary layer transition might prematurely shift upstream, potentially altering the flow characteristics. A Y+ value of 1 is thus maintained in the mesh refinement adjacent to the wall. This approach results in an initial layer thickness of 3.5e-6 m, which is indispensable for capturing both the laminar flow regime and the transition to the turbulent boundary layer with high fidelity. Moreover, the prismatic mesh layers are configured with a growth rate of 1.2, allowing for a smooth gradation in mesh density as we move away from the wall. This graded mesh structure extends outward to meet the interface seamlessly, optimizing the transition between the high-resolution near-wall mesh and the less dense outer mesh without introducing significant numerical artefacts.

2.3. Convergence analysis

2.3.1. Grid convergence

To assess mesh convergence, we adjusted the growth rate of the mesh surrounding the hydrofoil in the refinement region. We set the expansion rates of the grid layers around the hydrofoil to 1.4, 1.3, 1.2, and 1.1. Only the grid in the refinement region was modified, resulting in 33024, 35604, 40764, and 53664 elements of the refinement region grid for convergence verification. We then set the time step to 2.5e-5s. Table 1 summarizes the number of refinement meshes, maximum lift coefficients, and vortex shedding frequencies corresponding to the different expansion rates.

Presented in Table 1 are the comparative results of the maximum lift coefficients under four distinct grid configurations. These results demonstrate a converging trend in the lift forces, suggesting consistency across the varying mesh densities. As the grid expansion rate diminishes, a corresponding increment in the grid count is observed, which in turn leads to the stabilization of the vortex shedding frequency. Upon scrutinizing the data associated with grid expansion ratios of 1.1 and 1.2, minimal fluctuations are noted, thereby implying that the computed lift for these grid densities has reached a state of grid independence within the investigated parameters.

2.3.2. Time step convergence

According to the results of our study, we employed a grid of 40764 elements to investigate vortex shedding and tested different time steps to ensure convergence of our findings. Specifically, we reduced the time step of the simulation from 1e-4 to 2.5e-5 s. The lift coefficients and vortex shedding frequencies were recorded for different time steps in Table 2.

The data delineated in Table 2 reveal that the numerical values obtained across different iterations exhibit a high degree of similarity. It is especially noteworthy that the outcomes recorded at time steps of 2.5e-5 s and 1e-5 s display a striking proximity regarding both lift coefficient and vortex shedding frequency. This proximity suggests that convergence has been achieved at these time discretizations. In light of the computational efficiency, a time step of 2.5e-5 s was adjudicated as the optimal choice for the simulations, striking a balance between accuracy and computational resource expenditure.

Table 1
Convergence analysis of mesh.

Expansion rate	C_l(max)	Frequency (Hz)
1.4	0.07020	400
1.3	0.06960	430
1.2	0.07065	445
1.1	0.07230	440

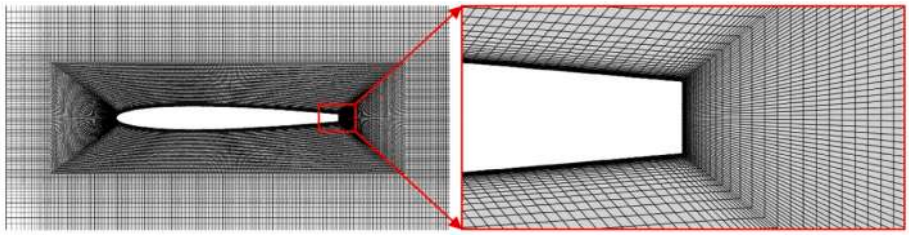

Fig. 4. Computational domain grid of NACA0009 hydrofoil.

Table 2
Convergence analysis of time step.

Time step (s)	C_l(max)	Frequency (Hz)
1e-4	0.07237	440
5e-5	0.07292	449
2.5e-5	0.07070	445
1e-5	0.07098	450

2.3.3. Viscous model

Based on our mesh and time step convergence analysis, we determined that the boundary layer mesh growth rate should be set to 1.2 and the time step to 2.5e-5 s. We verified the convergence of the *SST* $k-\omega$ with the γ transition model, transition *SST*, and LES models using these two parameters. Table 3 displays the comparison results, indicating no significant differences among the three models. As a result, we selected the *SST*$k-\omega$ for subsequent simulations because it can accurately compute the boundary layer flow of the structure and required fewer computational resources.

2.4. Model validation and error analysis

To accurately model the flow dynamics in our simulation, we recalculated the boundary layer thickness with Y+ values less than 1 for the flow velocity conditions employed. Table 4 details the vortex shedding frequencies derived at assorted flow velocities, as well as the relative errors between experimental and simulation results. Specifically, F_1 and F_2 represent the simulation results, with F_1 utilizing a transition model and F_2 not using a transition model. F_3 and F_4 represent experimental results (Ausoni et al., 2006), where F_3 is for a smooth hydrofoil, and F_4 is for a rough hydrofoil

Fig. 5 presents a comparison of the vortex frequencies in our CFD with those reported by Ausoni et al. (2006). Table 4 shows the specific simulation and experimental data along with their corresponding error analysis. The results indicate that the fluid simulation using the transition model aligns closely with the smooth hydrofoil experimental results, with a maximum error of 9.18% and a minimum error of 0.99%. The SST no-transition model simulation compares well with the rough leading edge experiments, with a maximum error of 15.30% and a minimum error of 6.21%.

Ausoni et al. attributed the observed differences between experimental outcomes for hydrofoils with smooth and rough leading edges to variations in the dynamics of the surrounding flow field. In fluid experiments, the rough leading edge of the hydrofoil caused the boundary layer transition into turbulence to occur at a position further upstream compared to smooth hydrofoils. This difference in the vortex shedding frequency between the two types of hydrofoils suggests a strong correlation between the onset of turbulence and the vortex shedding frequency. From simulation results, it can be seen that the SST turbulence model, when combined with transition equations, provides a more accurate description of the transitional flow state for smooth hydrofoils.

3. Results and discussion

3.1. The natural vortex shedding of hydrofoils

According to the results of the convergence analysis, we used a boundary layer mesh expansion rate of 1.2 and a time step of 2.5e-5s as

Table 3
Comparison of turbulence models.

Model	C_l(max)	Frequency (Hz)
SST $k-\omega$	0.0724	445
Transition SST	0.0729	430
Les	0.0707	400

Table 4
Vortex frequency at varying flow velocities.

Velocity	F_1 (Hz)	F_2 (Hz)	F_3 (Hz)	F_4 (Hz)	$\frac{\lvert F_1-F_3\rvert}{F_3}$	$\frac{\lvert F_2-F_4\rvert}{F_4}$
6 m/s	445	325	490	306	9.18%	6.21%
7 m/s	526	407	513	353	2.53%	15.30%
8 m/s	600	468	606	424	0.99%	10.38%
9 m/s	680	531	705	475	3.55%	11.79%
10 m/s	755	594	795	532	5.03%	11.65%

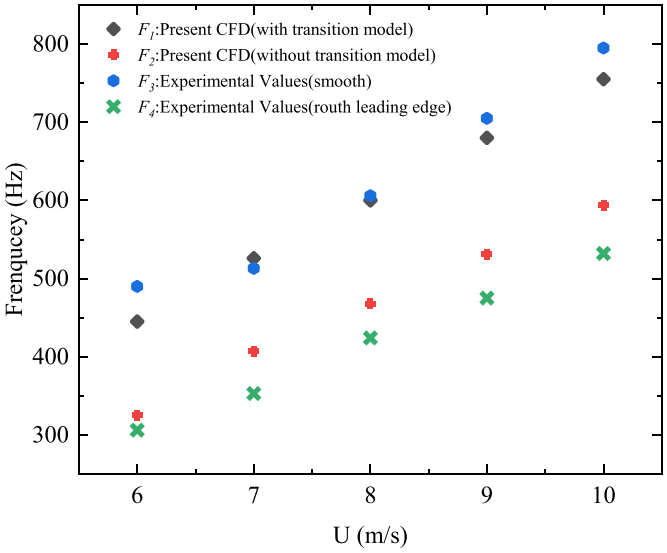

Fig. 5. Frequency of vortex shedding at different inflow velocities.

the computational parameters for the simulation using the SST $k-\omega$ model for fluid calculations. The flow velocity V_f was specified at 6 m/s. We obtained the mechanical coefficients of the hydrofoil with the dimensionless time quantity $t = TV_f/c$ defined as the horizontal coordinate from the fluid simulation and plotted the correlation curve.

Fig. 6 illustrates the dynamic changes in the Lift Coefficient (C_l) and Drag Coefficient (C_d) through the course of the simulation until a steady state is reached. Initially, the curves exhibit noticeable fluctuations, indicating a transient phase in the flow domain. During this period, the C_d curve is characterized by sizable variations, reflecting significant

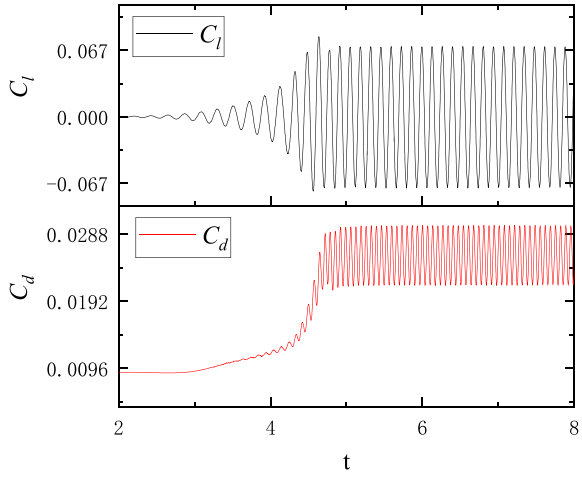

Fig. 6. Convergence-time history curve of lift coefficients C_l and drag coefficients C_d.

instability in dynamic drag force experienced by the model. Concurrently, the C_l curve displays a progressively intensifying oscillation pattern, signifying the developing lift force is undergoing considerable adjustments. As the simulation progresses, it is observed that both the C_l and C_d begin to exhibit reduced volatility; their respective curves start to smooth out, indicative of the flow settling into a more stable pattern. Eventually, the plots demonstrate that the computational domain achieves a steady state, characterized by minimal fluctuation in the coefficients. The steadying of the curves implies that the lift and drag forces have reached a consistent and predictable behavior. This steady-state region in the plots is critical for validating dynamic models and forms the basis for further computational analysis and optimization of dynamic performance.

Fig. 7 displays the PSD (Power Spectral Density) in the region of steady-state oscillations in lift and drag. From the spectral analysis, it is discernible that the lift force oscillates with a dominant frequency of approximately 445 Hz. This frequency is notably lower than that of the drag force oscillations, which are observed to be roughly twice as frequent. This disparity in oscillatory behavior can be attributed to the inherent nature of the vortical patterns shed from the hydrofoil. In essence, the generation of lift is associated with the formation and shedding of a pair of counter-rotating vortices, which together contribute to a single lift oscillation cycle. Contrastingly, the drag oscillations are tied directly to the shedding of individual vortices from each side of the hydrofoil's trailing edge. These shed vortices influence the force more frequently within the same timeframe, due to their successive detachment contributing to alternate low and high-pressure zones along the surface of the hydrofoil, resulting in the periodic force fluctuations.

Fig. 8 provides a crucial snapshot into the complex fluid dynamics experienced by the hydrofoil throughout one complete cycle of lift. By selecting four critical points in time—T1, T2, T3, and T4—within this cycle, we gain insights into the varying fluid mechanical states corresponding to the peaks and troughs in the lift coefficient. These selected instances allow us to capture and visualize the vorticity contours at each stage. Vorticity, a key fluid dynamic property that represents the local spinning motion of the fluid, is directly related to the generation of lift and is vividly depicted in Fig. 9 for each of these times.

At times T1 and T3, we observe strong vortical activities in close proximity to the hydrofoil. This is indicative of vigorous vortex shedding—where one vortex detaches from one side of the hydrofoil—altering the local flow velocity and thus generating significant pressure differences across the hydrofoil. Meanwhile, T2 and T4 represent moments in the cycle where the newly shed vortex interacts with the opposite-side shear layer, a phenomenon amplified through the

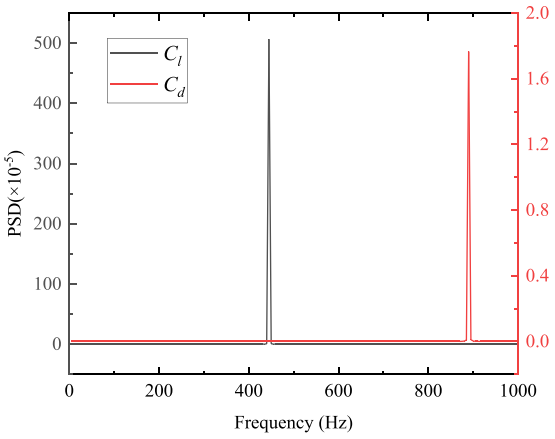

Fig. 7. Power Spectral Density of lift coefficients C_l and drag coefficients C_d curves.

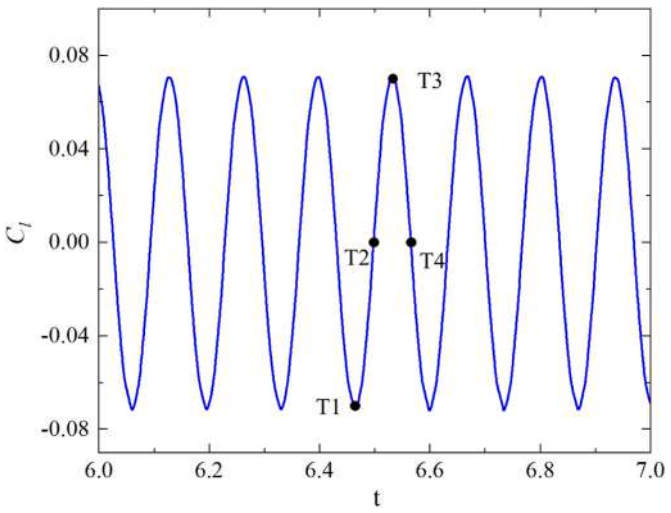

Fig. 8. Convergence region of lift coefficients C_l.

wake's suction effect. This interaction draws in the shear layer, driven by the momentum of the swirling fluid. During these interactions, the hydrofoil experiences the lowest lift forces in its cycle.

As depicted in Fig. 10, to gain further insights into the aerodynamics of the hydrofoil and specifically to ascertain vortex shedding frequency, a velocity monitoring point is strategically positioned in the wake of the hydrofoil. The rationale behind this placement is to directly measure the lateral velocity fluctuations, which are a physical manifestation of the vortex shedding phenomenon. The selection of a velocity monitoring point rather than direct measurement of lift fluctuations on the hydrofoil itself is a carefully considered choice. Measuring lift directly on the hydrofoil could lead to the introduction of additional drag forces, which may obscure the true nature of vortex shedding frequency. In contrast, the velocity monitoring point set within the hydrofoil's wake presents an opportunity to observe the tail-end results of the vortex shedding process. Any velocity fluctuations here can be more reliably attributed to the vortices shedding from the hydrofoil rather than to external forces or vibrations.

To facilitate the analysis and comparison of the monitored velocities, a dimensionless variable $U_y = V_y/V_f$ is defined. This non-dimensionalization serves to normalize the velocity data, allowing for a clear observation of the dynamic fluctuations against a baseline standard, unaffected by the absolute magnitudes of velocity, which is depicted in Fig. 11 through the time course curve of U_y.Fig. 12 complements this analysis by exhibiting the power spectral density (PSD) of U_y. The PSD provides a clear indication of the energy associated with varying frequency fluctuations. From the PSD plot, the dominant frequency can be identified, corresponding to the highest energy peak within the spectrum. This frequency aligns with the lift frequency detected by the hydrofoil and is, therefore, inferred to be the vortex shedding frequency.

3.2. Vortex shedding of vibrating hydrofoils

3.2.1. Prediction of locking boundaries by the wake oscillator model

Considering a dimensionless motion with amplitude y_0 and frequency ω, i.e., $y_0\cos(\omega t)$, the coupled displacement, velocity and acceleration models for the wake oscillator F in (10) are as follows:

$$\begin{aligned} F &= y_0\cos(\omega t) \\ F &= -y_0\omega\sin(\omega t) \\ F &= -y_0\omega^2\cos(\omega t) \end{aligned} \tag{18}$$

We chose an acceleration coupled model to study the impact of hydrofoil forced movement on near wake flow. The natural vortex frequency in the wake oscillator model is 445 Hz, and the damping factor ε

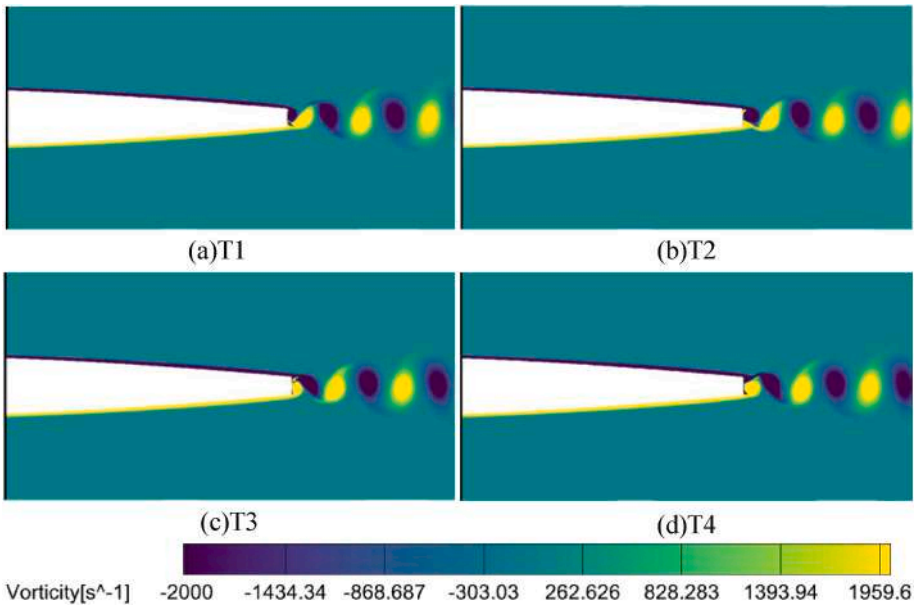

Fig. 9. Vortex shedding from the trailing edge (t = T1, T2, T3, T4).

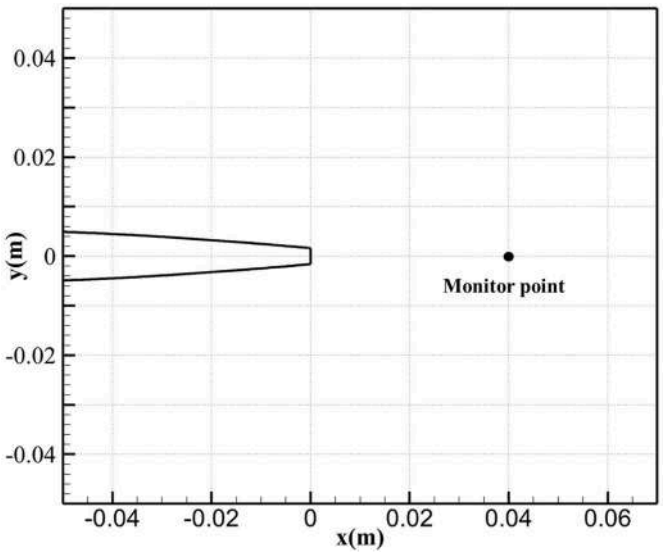

Fig. 10. Speed monitoring points at the trailing edge of the hydrofoil.

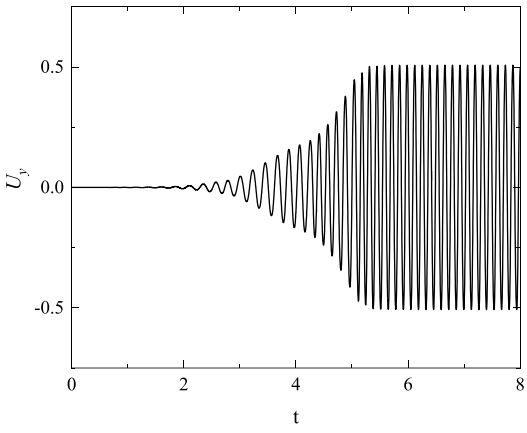

Fig. 11. Dimensionless transverse velocity U_y at the monitoring point.

is 0.2. The vibration frequency ω in the forcing term F is 1.1 times that of Ω_f, and the vibration parameters Ay_0/D are 0, 0.2 and 0.3. The time and FFt results of the wake trace variable q are calculated using the fourth-order Runge–Kutta method, as shown in Fig. 13.

When the vibration parameter Ay_0/D is 0, the wake variable q spontaneously generates stable fluctuations due to the influence of nonlinear damping, with the main frequency being 445 Hz. When the vibration parameter Ay_0/D is increased to 0.2, the time domain signal of the wake variable q is still periodic but not simple harmonic motion, and there are several secondary peaks in its spectrogram in addition to 445 Hz. When the vibration amplitude Ay_0/D is increased to 0.3, the wake fluctuations become more stable again, and their dominant frequency is 1.1times Ω_f, which is consistent with the structure's forced vibration frequency ω, indicating that locking occurs at this point.

We analyzed the lock-in boundary of the wake oscillator in parameter space (Ay_0/D, ω/Ω_f) for three coupling modes (see Fig. 14). The analysis was conducted for damping ratios ε set at values of 0.2, 0.3, and 0.4, to systematically gauge the wake oscillator's response under different levels of structural damping. In the absence of a definitive theoretical framework to guide the selection of the vibration parameters A, the explorative analysis proceeded on qualitative grounds. The resulting lock-in boundaries turned out to be significantly variant across the evaluated coupling modes. Asymmetry was noticed in the spatial extent of the lock-in boundaries across the different coupling scenarios. For the displacement coupling model, the height of the lock-in boundary on the higher frequency side ($\omega/\Omega_f > 1$) was found to surpass that on the lower frequency side ($\omega/\Omega_f < 1$). This asymmetry inverted when considering the acceleration and velocity coupling models, where the lock-in boundary was notably higher on the lower frequency side.

3.2.2. *Prediction of locking boundaries by fluid simulation models*

To elucidate the influence of the angle of attack on the lock-in behavior of vortex shedding, we have conducted simulations that specifically examine the hydrofoil's vortex patterns and their subsequent acoustic emissions when in a locked state. In all simulations, the hydrofoil moves forward at a speed of 6 m/s with a time step of 2.5e-5 s. The simulations commence from an initial condition of rest and persist

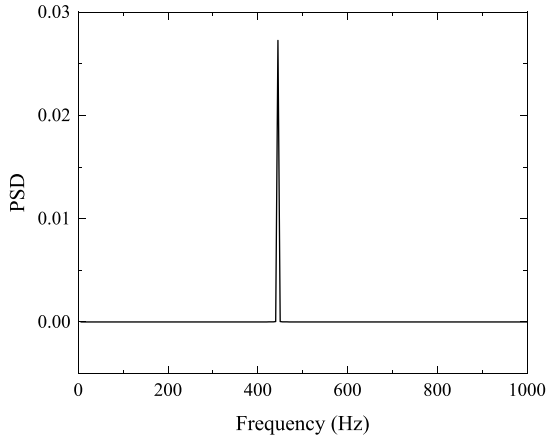

Fig. 12. Power spectral density of dimensionless transverse velocity U_y.

until a quasi-steady state is achieved. It is essential to note that due to the intrinsic complexities within the flow field, a considerable duration is needed for the attainment of stabilization. Therefore, the demarcated lock-in boundaries explicated in our study are better construed as approximations.

(1) Hydrofoil with $\alpha = 0°$.

In the numerical simulation carried out, the hydrofoil was positioned at a predetermined angle of attack, specified within our study scope. The vortex shedding frequency under the natural, non-vibration state is designated by the term Ω_f.The forced vibration frequencies to which the hydrofoil was subjected were 0.8, 0.9, 1.1, and 1.2 times " Ω_f" respectively. The primary objective was to achieve lock-in of the vortex shedding frequency, which necessitated precise modulation of the hydrofoil's vibration amplitude. To determine the lock-in condition and to avoid the complex effects of drag caused by structural vibrations, lateral velocity fluctuations U_y at a dedicated monitoring location were carefully observed. The criterion for lock-in was established based on the consistency of these velocity signatures with the hydrofoil's excitation frequency.

In Fig. 15, The observed characteristics of the lock-in boundary of the hydrofoil reveal an asymmetry, with a higher boundary on the right side, signifying that vortex shedding at higher frequencies necessitates larger structural amplitudes to achieve lock-in. This empirical result converges with theoretical insights advanced by the displacement coupling wake oscillator model.

The empirical data encapsulated in Fig. 16 delineate an inverse relationship between the degree of frequency lock-in and the dynamic performance of the hydrofoil. Specifically, as the frequency offset from the natural vortex shedding frequency augments, there is a proportional increase in the generated lift. Conversely, the drag coefficient shows a propensity for reduction.

Further visual analysis presented in Fig. 17 focuses on the pattern of vortex shedding from the hydrofoil's trailing edge when the system reaches a state of complete lock-in. It is observed that an increase in the locking frequency induces a more densely packed configuration of vortex structures. This compaction is attributed to the modulation of the vortical formation due to the hydrofoil's imposed vibrations, which seem to preemptively truncate the formation loop of the vortices. At $\omega/\Omega_f = 1.2$, the shedding takes on a distinctly coherent pattern, with vortices being released from the hydrofoil's trailing edge in near-paired synchrony.

(2) Hydrofoil with $\alpha = 6°$.

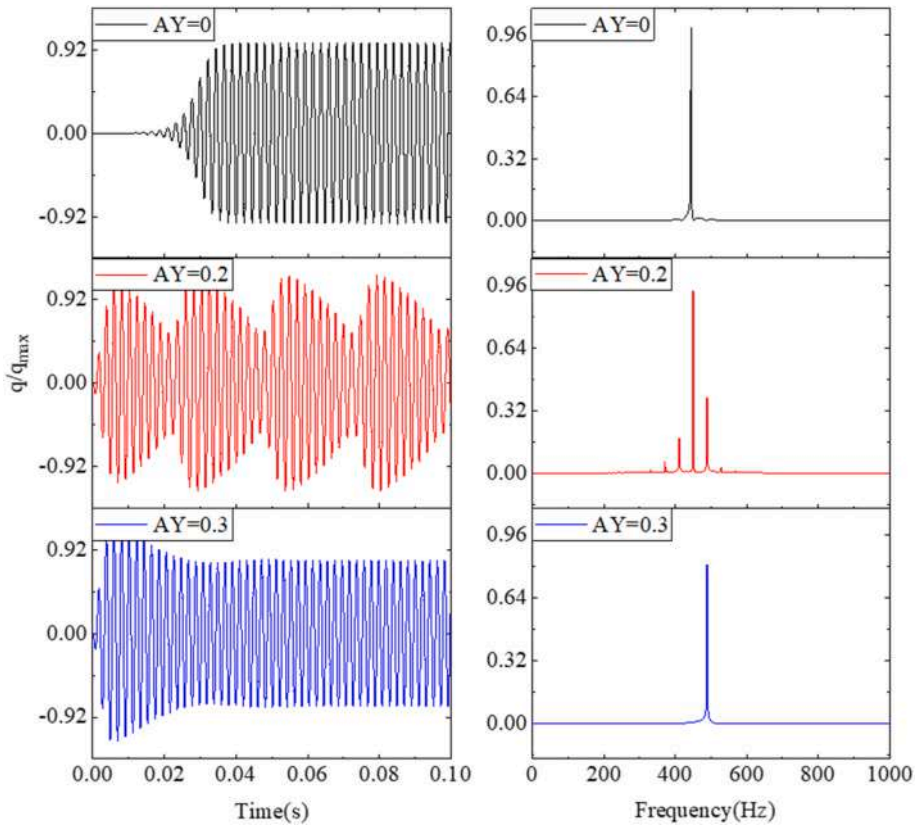

Fig. 13. Time and frequency domain characteristic curves of the wake variable q.

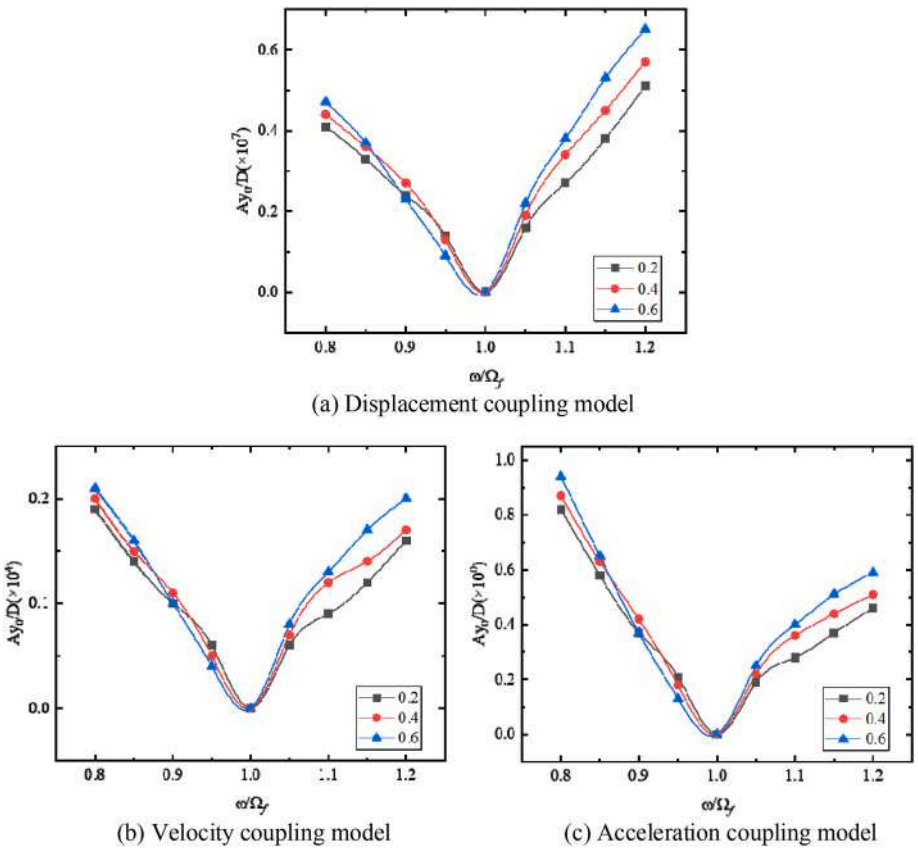

Fig. 14. Locking boundaries for different coupled models.

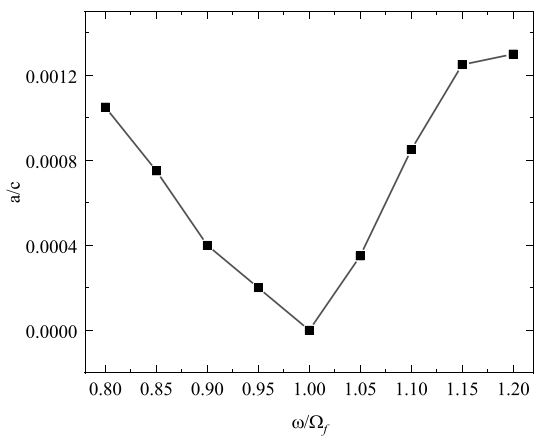

Fig. 15. Locking boundary for vortex shedding ($\alpha = 0^{\circ}$).

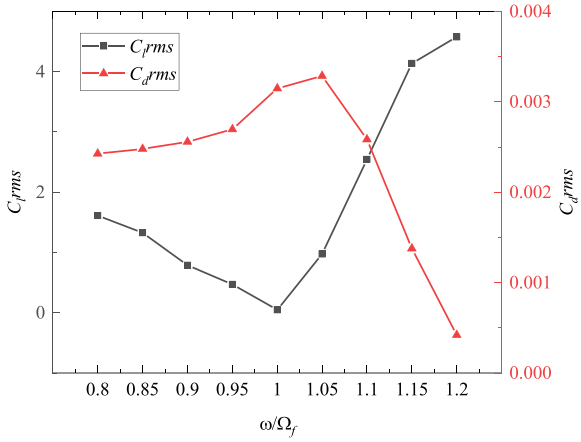

Fig. 16. $C_l rms$ and $C_d rms$ corresponding to locked boundaries ($\alpha = 0^{\circ}$).

Fig. 18 illustrates the wake vortex shedding configuration for the hydrofoil set at a 6-degree angle of attack, ensuring the absence of any externally imposed vibrational influence. A comparative observation reveals a disparate shedding pattern relative to that of the hydrofoil with a 0-degree angle of attack. Specifically, the vortex shedding for the hydrofoil at the 0-degree angle is observed to be more homogeneously apportioned on either side of the hydrofoil. In contrast, the hydrofoil posited at a 6-degree angle exhibits a vortex footprint on the upper surface that appears to be significantly more constricted. Velocity fluctuations U_y recorded at a designated monitoring point on the hydrofoil, angled within the constant flow field, alongside their corresponding Fourier transform analyses, are presented in Figs. 18 and 19. From the derived spectra (see Fig. 20), the natural shedding frequency is characterized as 353 Hz, substantiating that this frequency is lower when compared to that observed for the hydrofoil at 0-degree angle of attack.

Fig. 21 illustrates the lock-in boundary, alongside the associated non-dimensional amplitudes, as well as the effective coefficients of lift and drag for a hydrofoil at a 6-degree angle of attack. The lock-in boundary displayed demonstrates a resemblance to the characteristic boundary observed for the hydrofoil at a 0-degree angle of attack, as detailed in Fig. 15. This resemblance is particularly noted in the asymmetrical elevation of the right side of the boundary compared to the left. Such a

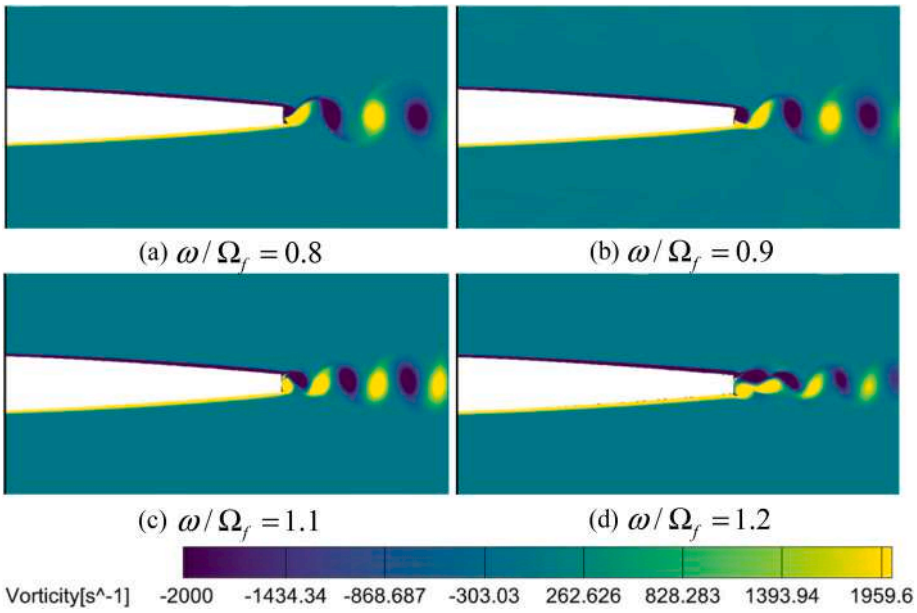

Fig. 17. Vortex shedding corresponding to different locking frequencies ($\alpha = 0^{\circ}$).

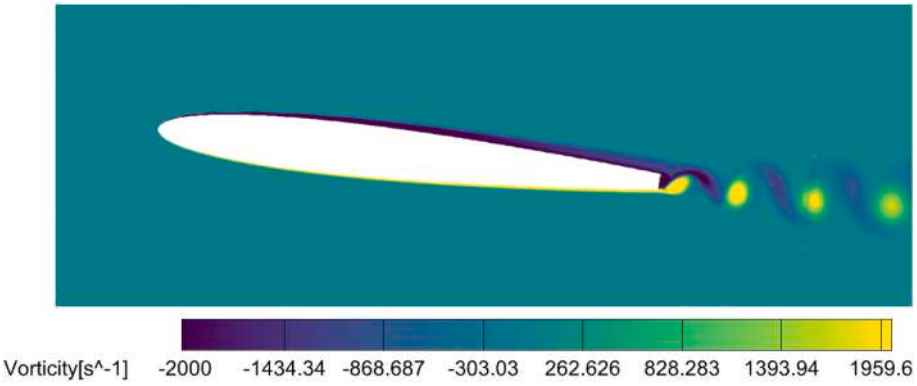

Fig. 18. Vortex shedding of a hydrofoil ($\alpha = 6^{\circ}$).

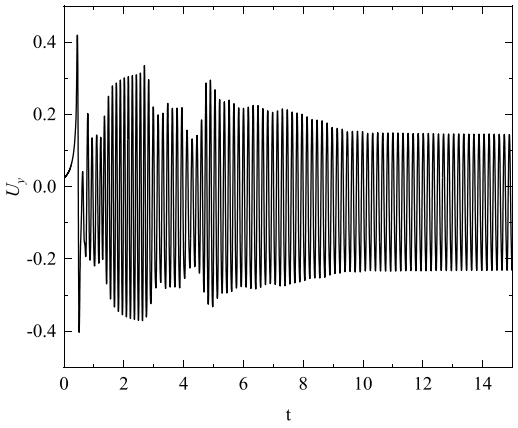

Fig. 19. Dimensionless transverse velocity U_y at the monitoring point ($\alpha = 6^{\circ}$).

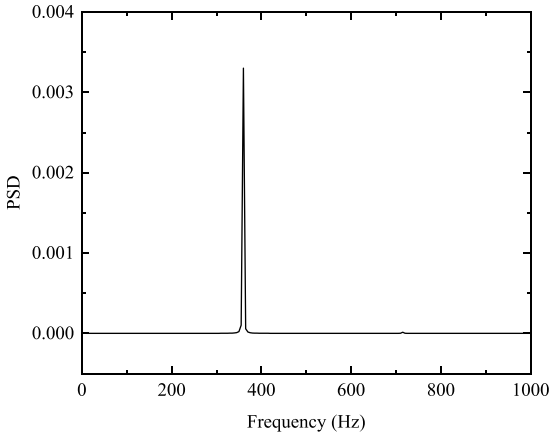

Fig. 20. Power spectral density of dimensionless transverse velocity U_y ($\alpha = 6^{\circ}$).

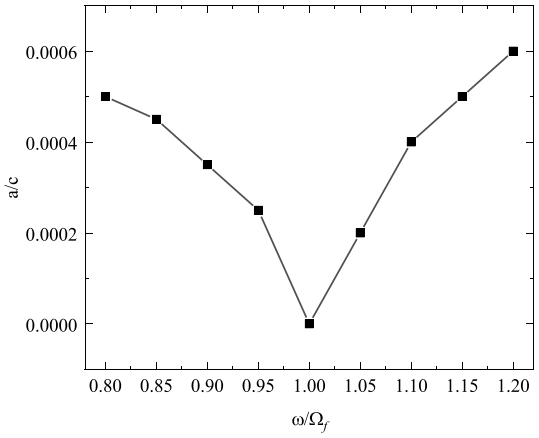

Fig. 21. Locking boundary for vortex shedding ($\alpha = 6^{\circ}$).

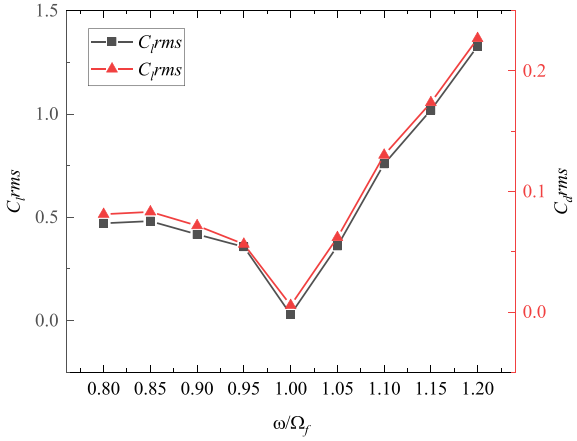

Fig. 22. Clrms and Cdrms corresponding to locked boundaries ($\alpha = 6^{\circ}$).

parallel substantiates the validity of the displacement coupling model's prognoses within the context of the wake oscillator framework. Notably, relative to the lock-in boundary pertaining to the 0-degree angle of attack hydrofoil, the 6-degree case evidences a requirement for a diminished structural amplitude to achieve locking. In addition,this condition is accompanied by an increase in both lift and drag coefficients as the lock-in frequency diverges from the natural vortex shedding frequency (see Fig. 22).

The phenomenon of complete lock-in is depicted in Fig. 23, wherein the corresponding vorticity field is shown. Within this state, a decrement in the fully locked frequency correlates to a reduction in the vortex arrangement density, indicating a more dispersed shedding pattern. This trend underscores the interconnectivity between the frequency of vortex shedding and the spatial distribution of vortices in the wake of a hydrofoil, especially under the influence of lock-in condition.

(3) Hydrofoil with $\alpha = 12^{\circ}$.

During the computational fluid dynamics simulations conducted for a hydrofoil set at a 12-degree angle of attack and absent any forced vibrations, the results indicated an absence of discernible vortex shedding phenomena. In an effort to delve deeper into these observations, the temporal resolution of the simulation was refined to a time step of 1e-6 s. Subsequent simulations, the outcomes of which are presented in Fig. 24 (1), reaffirmed the initial findings, showing the hydrofoil's wake to be devoid of significant vortex shedding activity.

Subsequently, a forced vibration characterized by a frequency of 200 Hz and an amplitude of 50 μm was applied to the hydrofoil. The flow field was then re-evaluated to discern the resultant patterns of vortex shedding, as presented in Fig. 24(2). Concurrently, lateral velocity fluctuations at a designated monitoring point were recorded, with the corresponding data illustrated in Fig. 25. Further investigation into the flow dynamics was conducted through a Fourier transform analysis, detailed in Fig. 26.

The recalculated results evidently showed pronounced vortex shedding from the oscillating hydrofoil. Moreover, the frequency of velocity fluctuations detected at the monitoring point corresponded directly with the externally imposed vibration frequency. This coherence between the vibration and vortex shedding frequencies can be attributed to the forced vibrations instigating perturbations within the shear layer at the hydrofoil's trailing edge. Such disturbances facilitate the encroachment of fluid from the shear layer into the center region of the trailing edge, leading to the formation of organized vortical structures. This process can be perceived as a result of the fluid-structure interaction wherein the hydrofoil's oscillation acts as a catalyst in the vortex generation mechanism.

3.2.3. *Acoustic characteristics analysis of vibrating hydrofoils*

In the context of low-speed conditions, turbulent noise contributions were determined to be minimal; therefore, the focus was placed exclusively on the solid surface of the hydrofoil as the principal source of noise (Khalid et al., 2019). To preclude any artefacts that could result from the placement of monitoring points too close to the transition wake area of the hydrofoil, the acoustic field observation points were strategically situated on a circular locus centered on the hydrofoil, with a radius extending 10 chord lengths (10C) from its midpoint. The primary monitoring point, situated directly astern of the hydrofoil's longitudinal axis, has been designated as R1. The subsequent points were arrayed in a counterclockwise configuration, each one distanced by an angular increment of 20° from its adjacent monitor, as depicted in Fig. 27. For consistency and comparability, the computational grid model and the temporal resolution parameters employed for the acoustic field simulations are maintained identical to those utilized in the prior aerodynamic simulations segment. This approach ensures coherence in the simulation framework, thereby enhancing the validity of the comparative analyses.

Fig. 28 portrays the comprehensive sound pressure level (SPL) directivity patterns for the hydrofoil. To facilitate a coherent comparative analysis, the SPL data are represented via polar plots scaled uniformly across all configurations. Observations of the sound propagation modalities reveal that the hydrofoil consistently exhibits dipole-like characteristics, regardless of whether it is in a state of natural or locked vortex shedding. The sound field distribution associated with the hydrofoil under locked conditions is characterized by a more pronounced fluctuation in the peak-to-valley amplitude of the SPL, principally attributed to the aerodynamic forces in play. The SPL along the vertical axis is influenced predominantly by the lift forces, whereas the SPL along the horizontal axis correlates substantially with the drag forces exerted on the hydrofoil. As demonstrated in Fig. 16, the phenomenon of lock-in, induced by forced vibrations of the hydrofoil, results in an augmented lift alongside a reduction in drag. It follows that there is an attendant elevation in the total SPL experienced laterally around the oscillating hydrofoil. Conversely, the SPL values detected in the horizontal plane are comparatively muted in relation to those of the hydrofoil in a quiescent state.

To delve deeper into the acoustical variations emanating from the hydrofoil's wake while under locked conditions, an analysis of the sound pressure level (SPL) spectrum was conducted at monitoring position R1. As depicted in Fig. 29, the dominant noise frequency from the hydrofoil

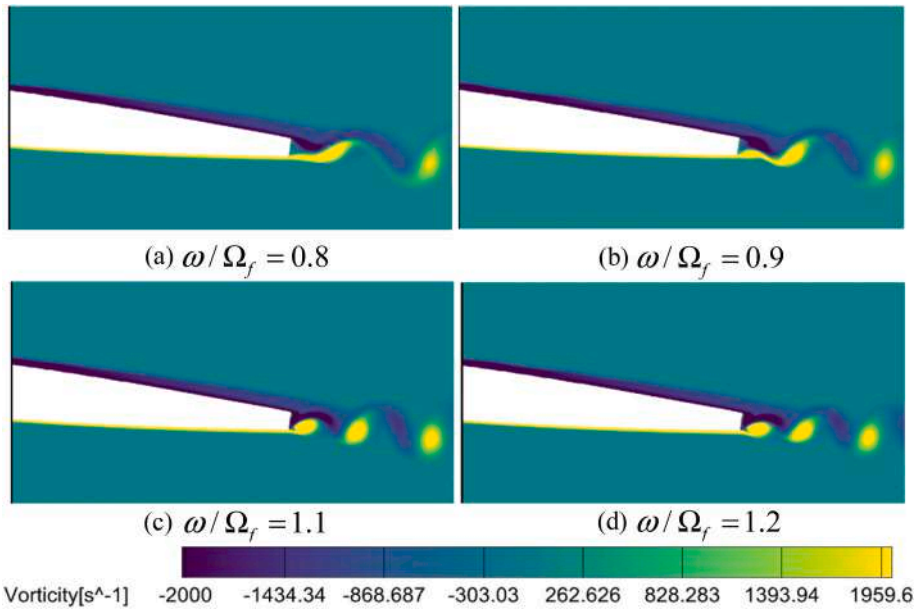

Fig. 23. Vortex shedding corresponding to different locking frequencies ($\alpha = 6^{\circ}$).

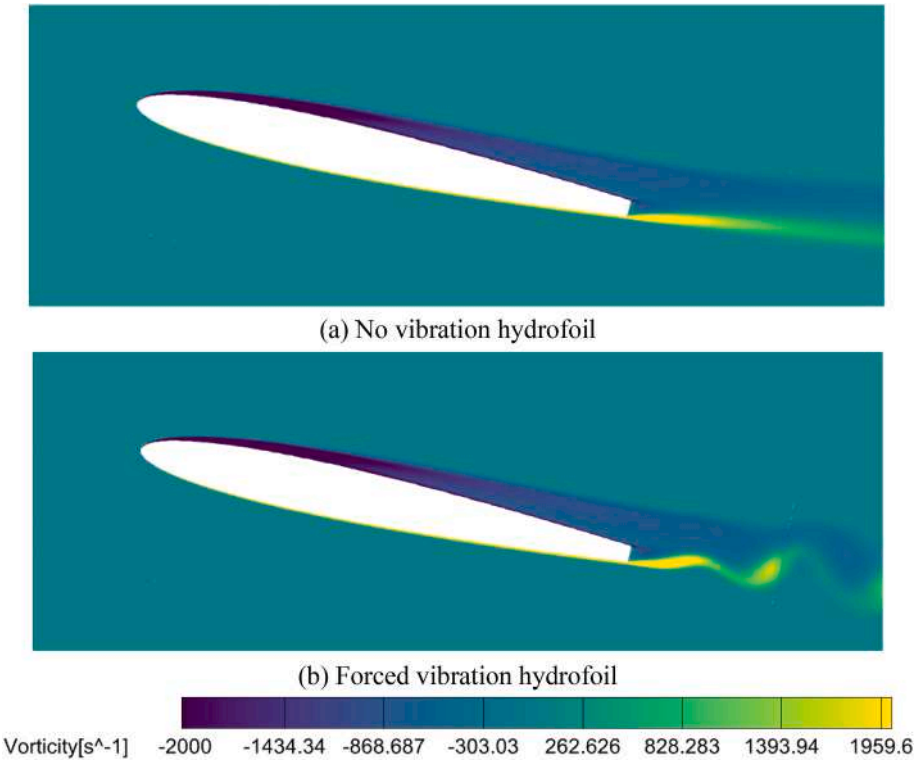

Fig. 24. Vortex shedding of a hydrofoil ($\alpha = 12^{\circ}$).

devoid of any vibration activity, as monitored in the direction of point R1, is observed to be twice the intrinsic vortex shedding frequency. This observation aligns with the principal frequency registered in the drag coefficient spectrum, as evidenced in Fig. 11. The correspondence between these frequencies suggests that fluctuations in drag have a predominant acoustic influence in the transverse wake direction. Upon the lock-in of the vibrating hydrofoil, there is a notable shift in the dominant noise frequency, moving to twice that of the lock-in frequency. In relation to the dominant noise frequency, the SPL in the wake's direction generally exhibits a diminutive by approximately 3 dB in comparison to the non-vibrating hydrofoil scenario. This reduction highlights the alterations in acoustical output that arise when the hydrofoil's vibratory state transitions into a lock-in with the vortex shedding.

A recalibration of the vibrational amplitude, A/C, was executed on the hydrofoil during the locked state by a diminutive amount of 0.0001, effectively unlocking the vortex shedding from its synchronized state. Subsequent to this adjustment, acoustic analyses were reconducted. Fig. 30 presents a juxtaposition of the locked and unlocked noise spectra, specifically at monitoring position R1, influenced by the hydrofoil's vortex shedding patterns. In evaluating the spectra, the noise profile in

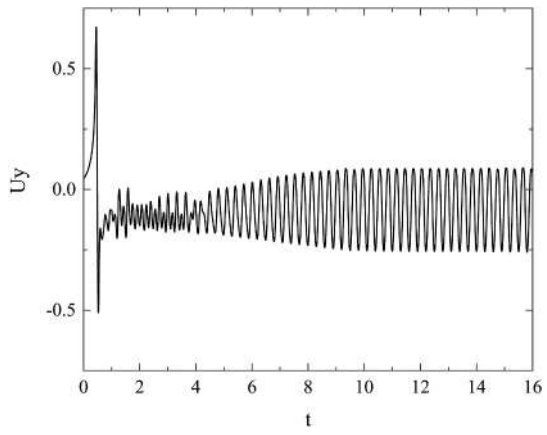

Fig. 25. Dimensionless transverse velocity *Uy* at the monitoring point (α = 12°).

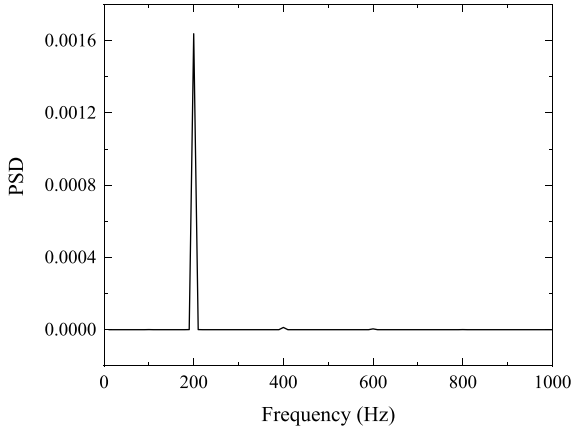

Fig. 26. Power spectral density of dimensionless transverse velocity *Uy* (α = 12°).

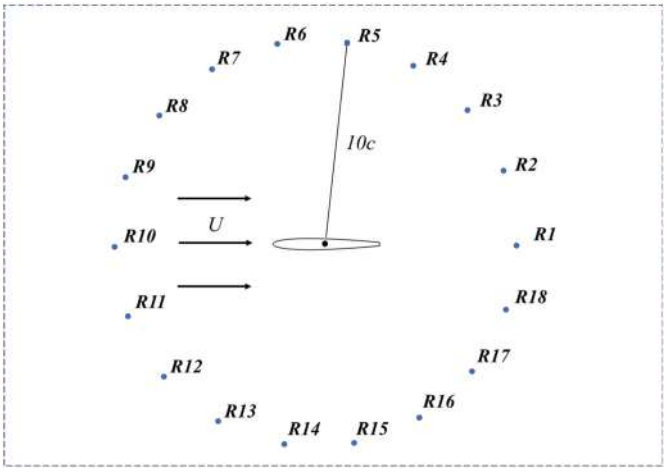

Fig. 27. Arrangement of the noise monitoring points.

the unlocked state manifests greater complexity within the 0–2000 Hz frequency domain, particularly pronounced in the low-frequency region spanning from 0 to 200 Hz, and also near the narrowband noise characteristics twice the frequency of the forced vibration. Despite the nuanced spectral changes between the locked and unlocked states, the peaks within the noise spectra for the unlocked condition match those of the locked state in terms of their magnitude. Consequently, the SPL associated with the noise peak in the unlocked condition remains 3 dB lower relative to the hydrofoil that was not subject to any vibrational input.

For future research initiatives, delving into the effects of active vibration on vortex shedding from three-dimensional (3-D) hydrofoils presents a promising trajectory. Current studies are predominantly concentrated on two-dimensional models and simulations, which somewhat constrains our comprehension of the complete and complex dynamics of hydrofoil flows. The 2-D models simplify the issue, facilitating computation and analysis, yet they overlook the influence of 3-D effects. Moreover, contemporary research relies heavily on numerical simulations, and for intricate fluid dynamic phenomena, the precision of simulation outcomes is often limited by the chosen models and computational techniques. Therefore, upcoming research will pivot towards employing fluid experimental platforms and Particle Image Velocimetry (PIV) technology to investigate hydrofoil flow control techniques. This approach not only provides a more tangible visualization of the flow field but also allows for experimental validation of the accuracy and applicability of simulation models. The scope of research will also be broadened to encompass asymmetric 3-D hydrofoil configurations, furnishing a more holistic understanding of flow dynamics and control mechanisms. Asymmetric hydrofoils are widely prevalent in design and application; however, their flow characteristics and control strategies are more complex and varied compared to symmetrical structures. By amalgamating experimental work with 3-D simulations, future studies can bridge the gaps present in current research, further advancing the development of hydrofoil design and flow control technologies.

4. Conclusion

In this study, the dynamics of vortex shedding from an actively vibrating hydrofoil were explored using the wake oscillator model and CFD simulations, and the frequency lock-in boundaries were assessed. The results indicate that the right-hand side of the lock-in boundary ($\omega/\Omega_f > 1$) consistently requires higher structural vibration amplitudes than the left-hand side ($\omega/\Omega_f < 1$), implying that increasing the frequency of vortex shedding necessitates an increase in structural vibration amplitude. Since this phenomenon is present in both the displacement coupling model within the wake oscillator model and the CFD, the model can be used to describe the wake oscillation characteristics of an actively vibrating hydrofoil as an alternative to fluid simulations. Furthermore, the acoustical characteristics downstream of the hydrofoil were also studied. When the frequency of vortex shedding is synchronized with the frequency of the hydrofoil's active vibration, a significant shift occurs in the dominant frequency of the far-field noise at the trailing edge of the hydrofoil, and the noise peak is also reduced by about 3 dB. This provides a research foundation for the topic of actively modulating noise by vibrating hydrofoils.

CRediT authorship contribution statement

Pengxiang Zhao: Writing – review & editing, Writing – original draft, Visualization, Investigation, Formal analysis, Conceptualization. **Jinliang Wu:** Writing – review & editing, Investigation, Data curation. **Xudong Zhang:** Writing – review & editing, Formal analysis. **Xin Lan:** Writing – review & editing, Validation, Methodology, Data curation. **Jinsong Leng:** Writing – review & editing, Investigation, Conceptualization. **Yanju Liu:** Writing – review & editing, Investigation, Conceptualization.

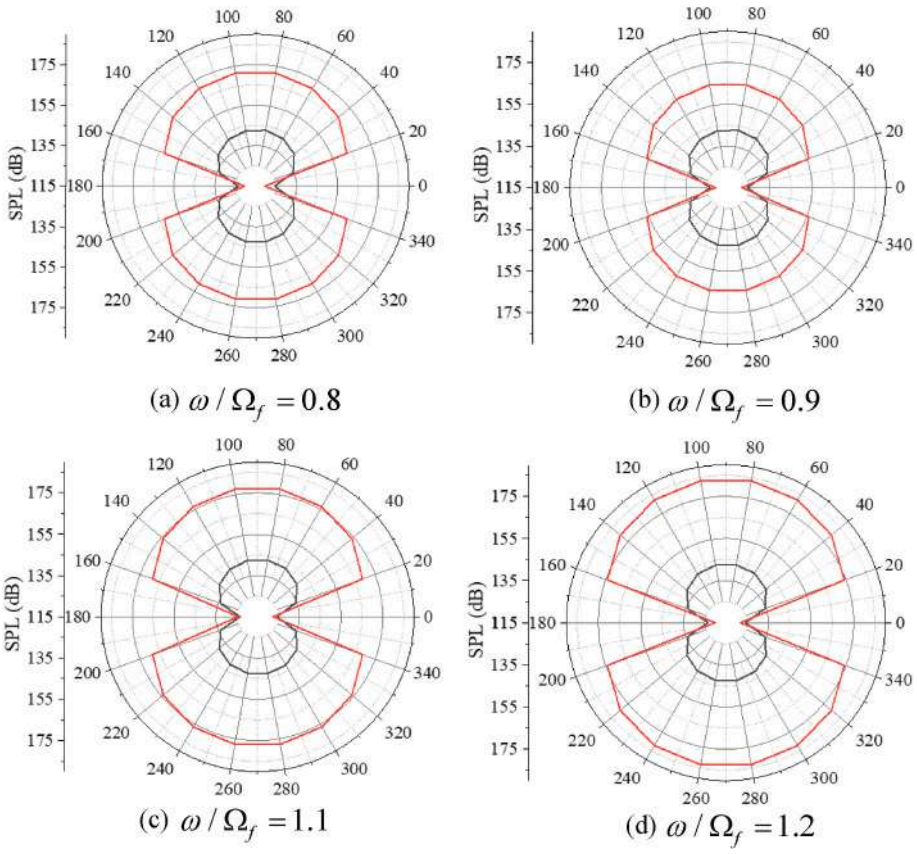

Fig. 28. Directivity of the hydrofoil sound pressure levels.

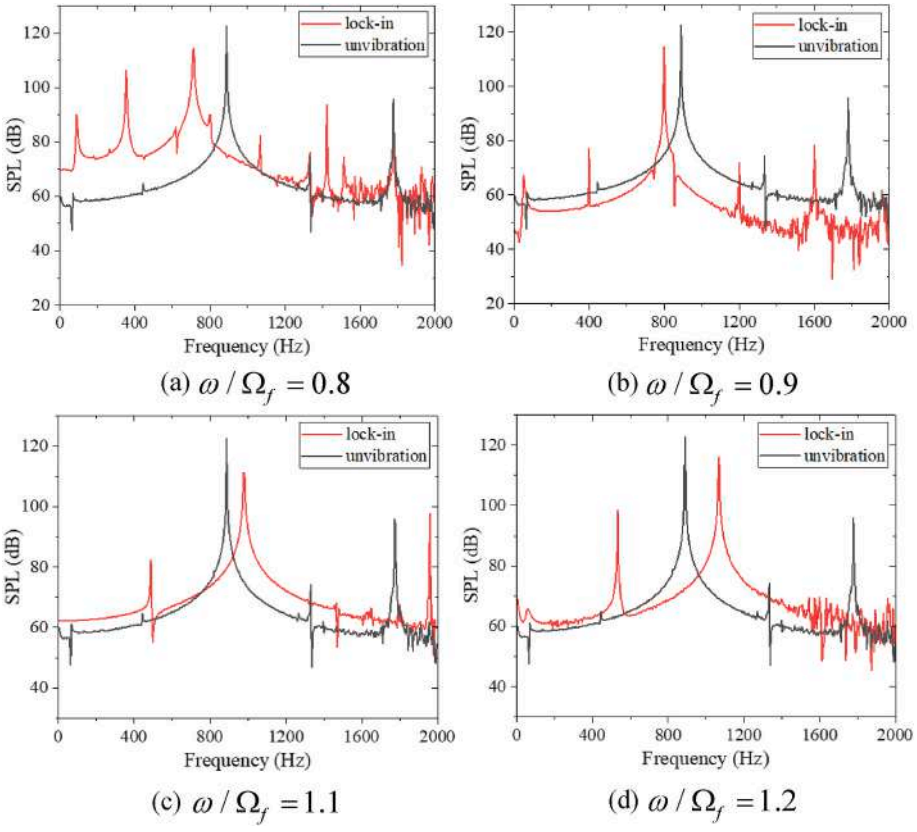

Fig. 29. Sound pressure level spectrum at point R1 corresponding to natural and locked vortex shedding.

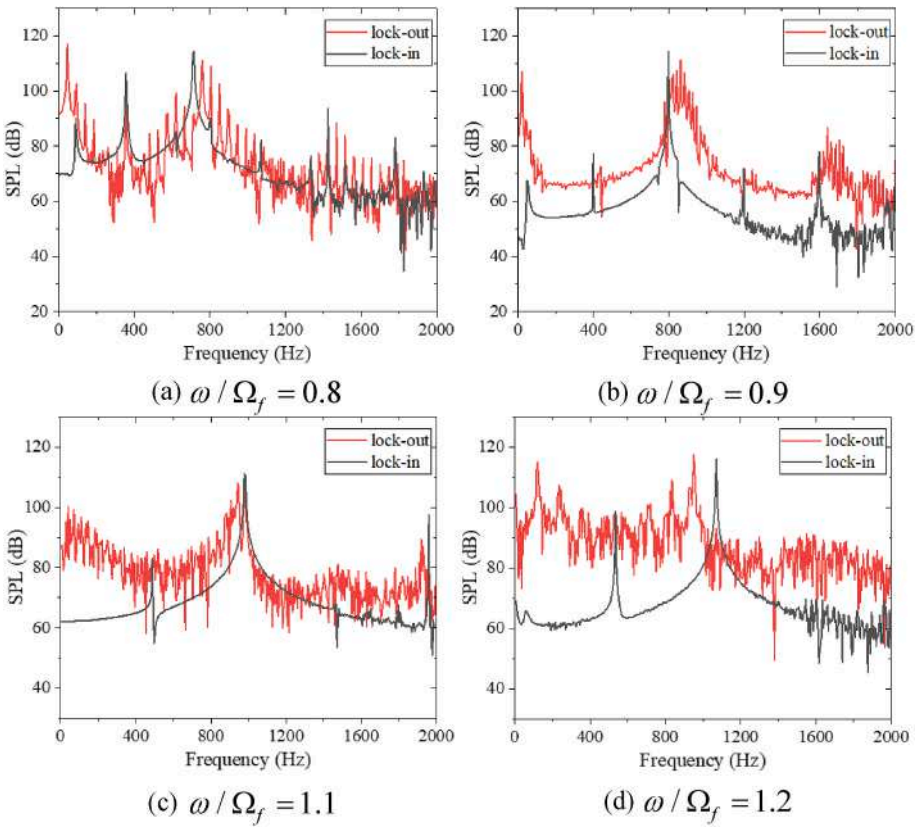

Fig. 30. Sound pressure level spectrum at the R1 point corresponding to the vortex shedding lock-in and lock-out.

Declaration of competing interest

We declare that we do not have any commercial or associative interest that represents a conflict of interest in connection with the work submitted.

Data availability

The authors do not have permission to share data.

Acknowledgment

The authors wish to acknowledge the support given by the National Natural Science Foundation of China [Grant no.12072094 and 12272113].

References

Ausoni, P., Farhat, M., Ait Bouziad, Y., Kueny, J.-L., Avellan, F., 2006. Kármán vortex shedding in the wake of a 2D hydrofoil: measurement and numerical simulation. IAHR Int. Meeting of WG on Cavitation and Dynamic Problems in Hydraulic Machinery and Systems.

Bishop, R.E.D., Hassan, A., 1964. The lift and drag forces on a circular cylinder oscillating in a flowing fluid. Proc. Roy. Soc. Lond. Math. Phys. Sci. 277 (1368), 51–75.

Blevins, R., 1990. Flow-Induced Vibrations. Van Nostrand Reinhold, New York.

Bourgoyne, D.A., Ceccio, S.L., Dowling, D.R., 2005. Vortex shedding from a hydrofoil at high Reynolds number. J. Fluid Mech. 531, 293–324.

Du, Z., Zhu, H., Tang, Y., 2023. Eigenwave analysis of vortex-induced vibrations on long cylinders in sheared flows. Ocean Eng. 287, 115714.

Ducoin, A., Astolfi, J.A., Gobert, M.-L., 2012. An experimental study of boundary-layer transition induced vibrations on a hydrofoil. J. Fluid Struct. 32, 37–51.

Gao, C., Zhang, W., Li, X., Liu, Y., Quan, J., Ye, Z., Jiang, Y., 2017. Mechanism of frequency lock-in in transonic buffeting flow. J. Fluid Mech. 818, 528–561.

Gerrard, J., 1966. The mechanics of the formation region of vortices behind bluff bodies. J. Fluid Mech. 25 (2), 401–413.

Griffin, O.M., 1995. A note on bluff-body vortex formation. J. Fluid Mech. 284, 217–224.

Hu, J., Wang, Z.B., Chen, C.G., Guo, C.Y., 2020. Vortex shedding simulation of hydrofoils with trailing-edge truncation. Ocean Eng. 214.

Huang, Z., Xiong, Y., Xu, Y., 2019. The simulation of deformation and vibration characteristics of a flexible hydrofoil based on static and transient FSI. Ocean Eng. 182, 61–74.

Khalid, M.S.U., Akhtar, I., Wu, B.X., 2019. Quantification of flow noise produced by an oscillating hydrofoil. Ocean Eng. 171, 377–390.

Koopmann, G., 1967. The vortex wakes of vibrating cylinders at low Reynolds numbers. J. Fluid Mech. 28 (3), 501–512.

Krenk, S., Nielsen, S.R., 1999. Energy balanced double oscillator model for vortex-induced vibrations. J. Eng. Mech. 125 (3), 263–271.

Lee, S.-J., Lee, J.-H., Suh, J.-C., 2016. Numerical investigation on vortex shedding from a hydrofoil with a beveled trailing edge. Model. Simulat. Eng. 2015, 9-9.

Liu, G., Yu, Y.L., Tong, B.G., 2012. Optimal energy-utilization ratio for long-distance cruising of a model fish. Phys. Rev. 86 (1).

Liu, H., Wassersug, R.J., Kawachi, K., 1996. A computational fluid dynamics study of tadpole swimming. J. Exp. Biol. 199 (6), 1245–1260.

Muhammad, Z., Alam, M.M., Ji, C.N., Zhu, H.J., Noack, B.R., 2022. Asymmetric wake, origin, generation, and suppression behind asymmetrically pitching hydrofoil. Ocean Eng. 266.

Nagarathinam, D., Hong, J.W., Ahn, B.K., Park, C., Kim, G.D., Moon, I.S., 2022. Dynamics of tip vortex flow over three dimensional hydrofoils by LDV measurements. Ocean Eng. 266.

Ni, Z., Dhanak, M., Su, T.-c., 2019. Performance of a slotted hydrofoil operating close to a free surface over a range of angles of attack. Ocean Eng. 188, 106296.

Qin, G., Zhang, H., Li, D., 2023. Numerical study on vortex induced vibration of hydrofoils with trailing-edge truncation. Ocean Eng. 275, 114083.

Smith, S.M., Brandner, P.A., Pearce, B.W., Venning, J.A., Moreau, D.J., Clarke, D.B., 2021. Steady and unsteady loading on a hydrofoil immersed in a turbulent boundary layer. J. Fluid Struct. 102, 103225.

Smith, S.M., Venning, J.A., Pearce, B.W., Young, Y.L., Brandner, P.A., 2020a. The influence of fluid–structure interaction on cloud cavitation about a flexible hydrofoil. Part 2. J. Fluid Mech. 897, A28.

Smith, S.M., Venning, J.A., Pearce, B.W., Young, Y.L., Brandner, P.A., 2020b. The influence of fluid–structure interaction on cloud cavitation about a stiff hydrofoil. Part 1. J. Fluid Mech. 896, A1.

Tokumaru, P., Dimotakis, P., 1991. Rotary oscillation control of a cylinder wake. J. Fluid Mech. 224, 77–90.

Wang, H.L., Zheng, X.B., Pröbsting, S., Hu, C.H., Wang, Q., Li, Y., 2023. An unsteady RANS simulation of the performance of an oscillating hydrofoil at a number. Ocean Eng. 274.

Warui, H., Fujisawa, N., 1996. Feedback control of vortex shedding from a circular cylinder by cross-flow cylinder oscillations. Exp. Fluid 21 (1), 49–56.

Williams, D.R., Mansy, H., Amato, C., 1992. The response and symmetry properties of a cylinder wake subjected to localized surface excitation. J. Fluid Mech. 234, 71–96.
Williamson, C.H., Roshko, A., 1988. Vortex formation in the wake of an oscillating cylinder. J. Fluid Struct. 2 (4), 355–381.
Ye, C., Wang, F., Wang, C., van Esch, B.P., 2020a. Assessment of turbulence models for the boundary layer transition flow simulation around a hydrofoil. Ocean Eng. 217, 108124.
Ye, C.L., Wang, F.J., Wang, C.Y., van Esch, B.P.M., 2020b. Assessment of turbulence models for the boundary layer transition flow simulation around a hydrofoil. Ocean Eng. 217.
Zeng, Y., Yao, Z., Zhou, P., Wang, F., Hong, Y., 2019. Numerical investigation into the effect of the trailing edge shape on added mass and hydrodynamic damping for a hydrofoil. J. Fluid Struct. 88, 167–184.
Zhao, H., Ding, H., Wang, C., Li, K., Wang, G., Ren, B., 2023. Vortex-induced vibration at low Reynolds numbers: vortex shedding modes transitions. Ocean Eng. 288, 115931.
Zobeiri, A., Ausoni, P., Avellan, F., Farhat, M., 2012. How oblique trailing edge of a hydrofoil reduces the vortex-induced vibration. J. Fluid Struct. 32, 78–89.